B.2.4 Example 1: L-shape domain problem

The first numerical example deals with a problem whose exact solution u is known. The advantage of such examples is that the approximation error $e_{h,p}(\boldsymbol{x}) = u(\boldsymbol{x}) - u_{h,p}(\boldsymbol{x})$ can be calculated exactly in the whole domain Ω. We consider a domain $\Omega \subset \mathbb{R}^2$ with a re-entrant corner, shown in Fig. B.2.

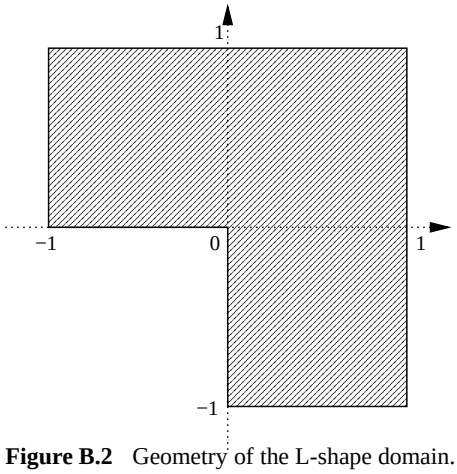

Figure B.2 Geometry of the L-shape domain.

Solved is the equation $-\Delta u = 0$ in Ω, equipped with the Dirichlet boundary conditions

$$u(\boldsymbol{x}) = R(\boldsymbol{x})^{2/3} \sin(2\theta(\boldsymbol{x})/3 + \pi/3) \qquad \text{for all } \boldsymbol{x} \in \partial\Omega.$$

Here $R(\boldsymbol{x})$ and $\theta(\boldsymbol{x})$ are the standard spherical coordinates in the plane. The exact solution has the form

$$u(\boldsymbol{x}) = R(\boldsymbol{x})^{2/3} \sin(2\theta(\boldsymbol{x})/3 + \pi/3) \qquad \text{for all } \boldsymbol{x} \in \Omega.$$

The magnitude of the gradient $|\nabla u|$ of the exact solution (whose calculation is left to the reader as an exercise) has a singularity at the re-entrant corner. This behavior is usual for second-order elliptic problems in domains with re-entrant corners, and it makes their numerical solution challenging. This phenomenon, despite being very local, is a significant source of error. The error can be measured in a variety of different ways. The H^1-norm

$$\|e_{h,p}\|_{H^1(\Omega)} = \left(\int_\Omega |u - u_{h,p}|^2 + |\nabla u - \nabla u_{h,p}|^2 \, \mathrm{d}\boldsymbol{x} \right)^{\frac{1}{2}}$$

is a natural choice from the point of view of the weak formulation of the problem. The L^∞-norm

$$\|e_{h,p}\|_{L^\infty(\Omega)} = \sup_{\boldsymbol{x} \in \Omega} |u(\boldsymbol{x}) - u_{h,p}(\boldsymbol{x})|,$$

on the other hand, gives the maximum difference of u and $u_{h,p}$. We use the H^1-norm in what follows. The problem was solved twice, using the piecewise-linear FEM and the hp-FEM. In both cases it was our goal to attain the best possible accuracy using the fewest possible degrees of freedom. The solution, gradient of the solution and the meshes are shown in Figs. B.3 – B.7. After that we compare the efficiency of the piecewise-linear FEM and the hp-FEM in Table B.1.

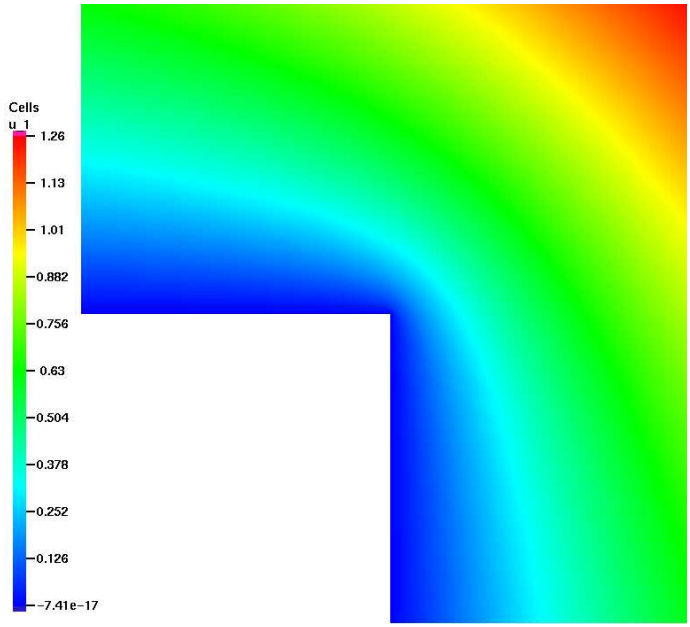

Figure B.3 The exact solution of the L-shape domain problem.

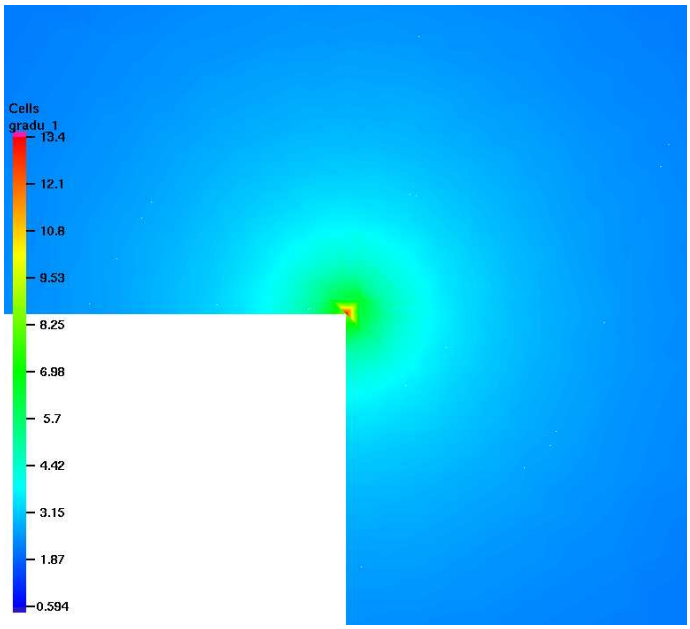

Figure B.4 Detail view of $|\nabla u_{h,p}|$ at the re-entrant corner (zoom = 70).

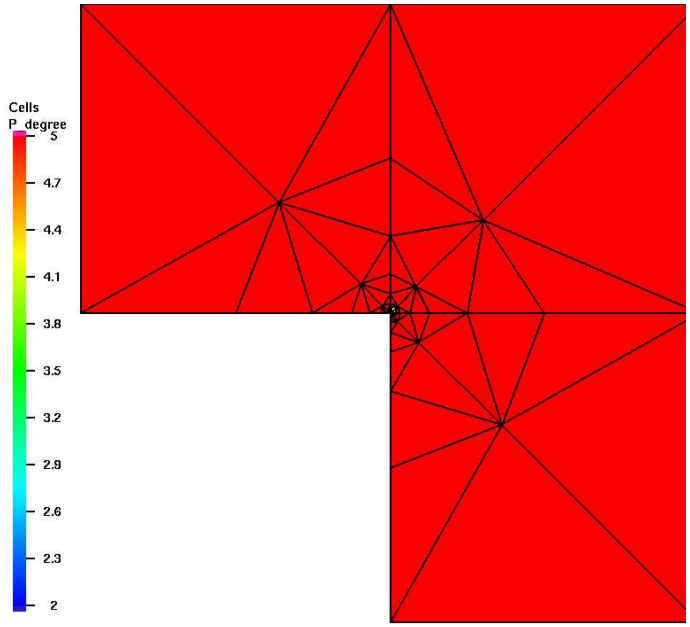

Figure B.5 The hp-mesh. Large fifth-order elements are used far from the singularity, small quadratic elements cover the vicinity of the re-entrant corner.

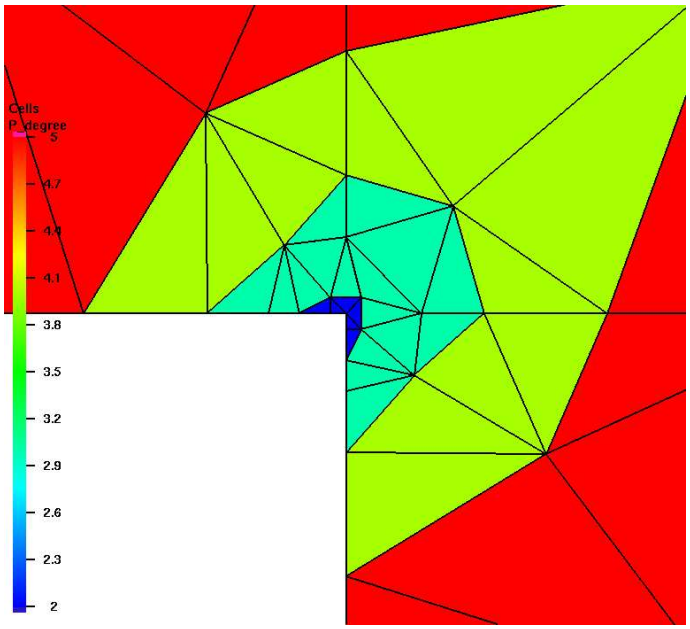

Figure B.6 The hp-mesh - detail of the re-entrant corner (zoom = 70).

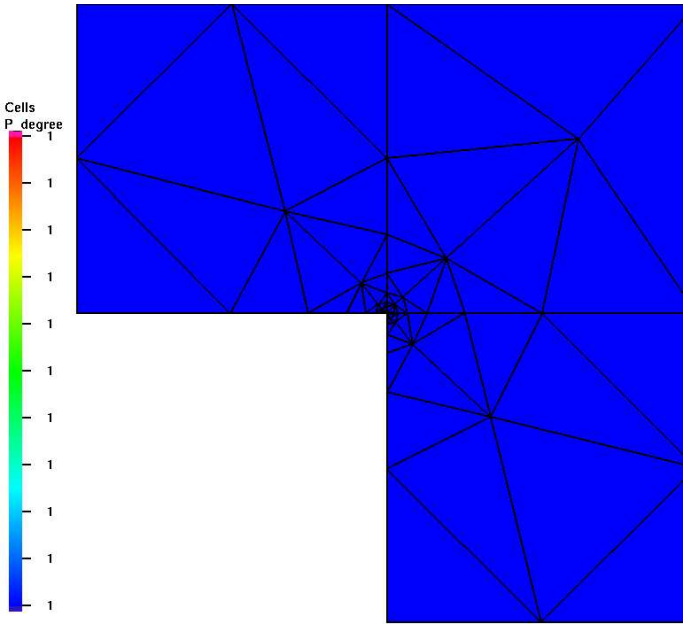

Figure B.7 The piecewise-linear mesh. This mesh was uniformly refi ned for the computation in order to reach the prescribed accuracy (each edge was subdivided into 60).

An efficiency comparison of the piecewise-linear FEM and hp-FEM is shown in Table B.1. Both computations, as well as all other computations shown in the following, were performed using our modular FEM system HERMES under identical conditions on a desktop Linux PC with a 3 GHz Pentium 4 processor and 2 GB of memory. The piecewise-linear FEM was obtained by setting the polynomial degree to $p := 1$ in all elements.

	linear elements	hp-elements
DOF	143161	839
Error	0.1876 %	0.1603 %
Iterations	421	30
CPU time	**2.1 min.**	**0.35 sec.**

Table B.1 Comparison of the number of DOF, relative error in the H^1-norm, number of iterations of the matrix solver and the CPU-time.

Acknowledgment We use the following public-domain software tools:

- The triangular mesh generator Triangle [107] by Richard Shewchuk (see `http://www-2.cs.cmu.edu/~quake/triangle.html`)
- The visualization tool General Mesh Viewer (GMV) by Frank Ortega (see `http://www-xdiv.lanl.gov/XCM/gmv/GMVHome.html`)

B.2.5 Example 2: Insulator problem

This time it is our goal to calculate the distribution of the electric field induced by an insulated conductor in the vicinity of a point where the conductor leaves the wall. The computational domain $\Omega \subset \mathbb{R}^2$ corresponding to this axisymmetric problem is depicted in Fig. B.8.

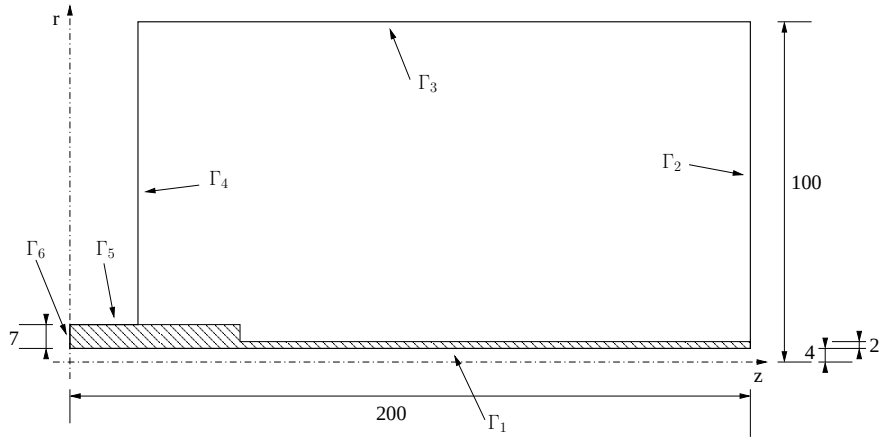

Figure B.8 Computational domain (all measures are in millimeters).

The wall itself, where we are not interested in the solution, is not included in the domain Ω. The same holds for the conductor at the horizontal axis of symmetry. Both the wall and the conductor are handled via suitable boundary conditions (to be defined below). The hatched subdomain $\Omega_2 \subset \Omega$ represents the insulator with the relative permittivity $\epsilon_r = 10$. The relative permittivity in the rest of the domain is $\epsilon_r = 1$. This problem is more difficult compared to the previous one, because in addition to a re-entrant corner there is a material interface in the domain along which the electric field $\boldsymbol{E}$ is discontinuous (i.e., across which the scalar potential φ has a significant jump in the derivative). Solved is the standard potential equation of electrostatics (7.27) in cylindrical coordinates, equipped with the following boundary conditions:

$$\varphi = 220 \text{ V} \qquad \text{on } \Gamma_1,$$

$$\varphi = 0 \text{ V} \qquad \text{on } \Gamma_4 \cup \Gamma_5,$$

and

$$\frac{\partial \varphi}{\partial \boldsymbol{\nu}} = 0 \qquad \text{on } \Gamma_2 \cup \Gamma_3 \cup \Gamma_6.$$

Again we compare the results obtained by means of the piecewise-linear FEM and hp-FEM. The solution, gradient of the solution and the meshes are shown in Figs. B.9 – B.13. An efficiency comparison is presented in Table B.2.

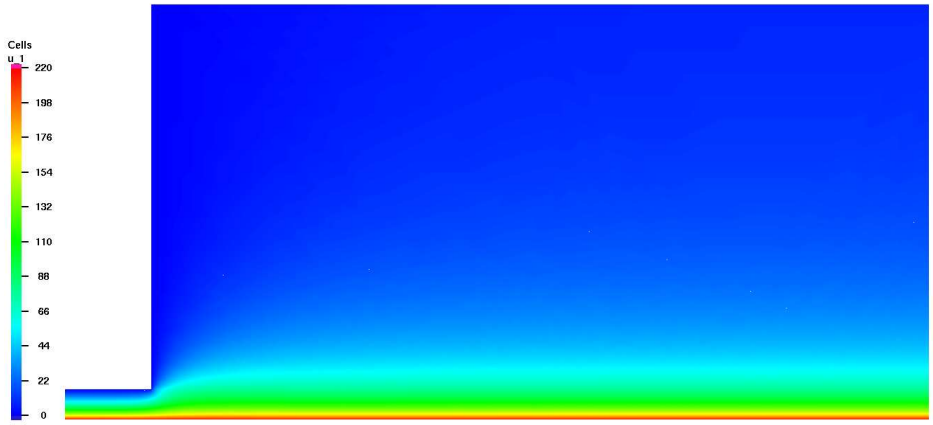

Figure B.9 Solution of the insulator problem (electric potential φ).

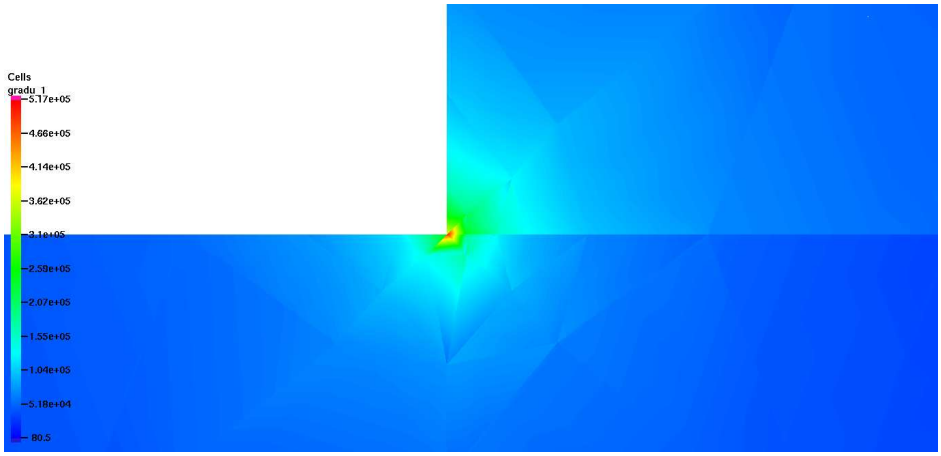

Figure B.10 Detail of the singularity of $|\boldsymbol{E}| = |-\nabla\varphi|$ at the re-entrant corner, and the discontinuity along the material interface (zoom = 1000).

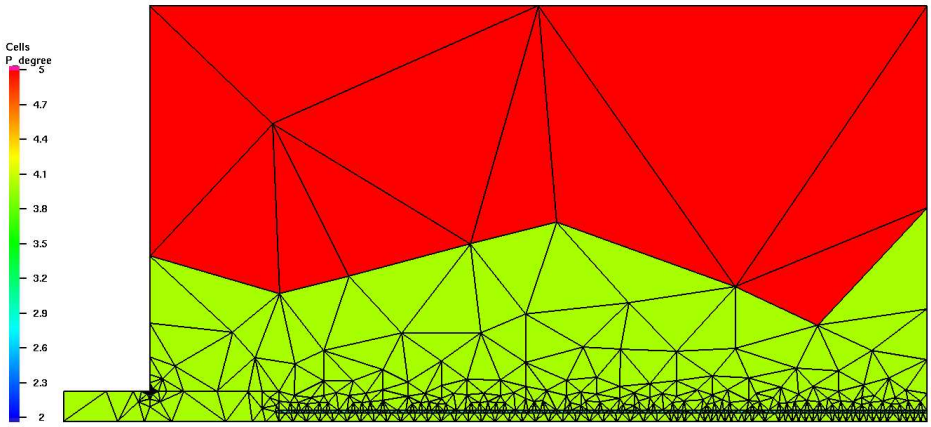

Figure B.11 The hp-mesh – global view. Large fi fth-order elements are used far from the singularity and material interface, small quadratic elements are placed close to the re-entrant corner and the material interface

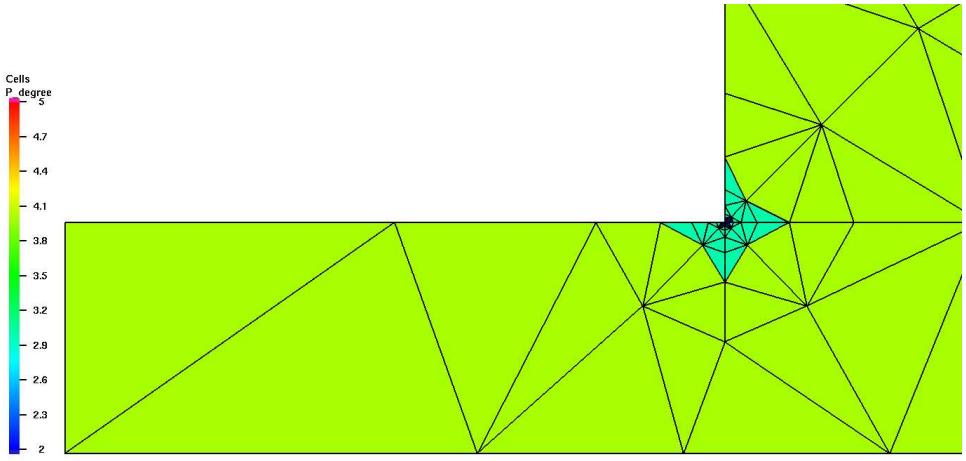

Figure B.12 The hp-mesh – detail of the re-entrant corner (zoom = 1000).

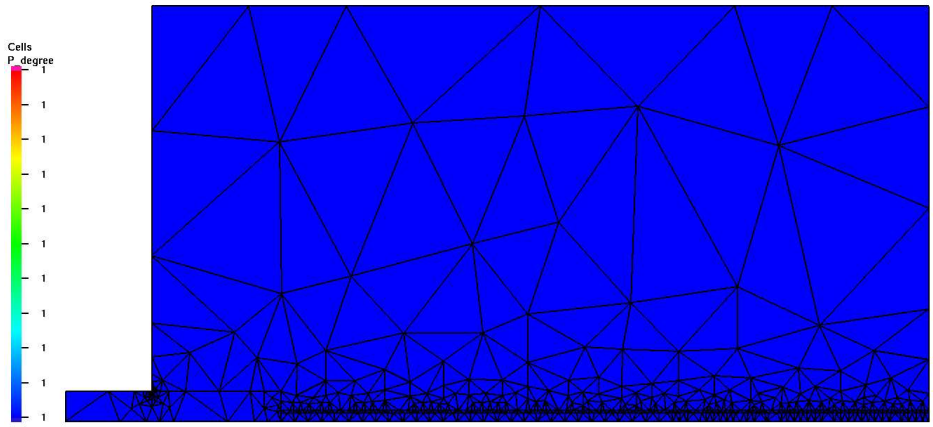

Figure B.13 The piecewise-linear mesh. This mesh was uniformly refined for the computation in order to achieve the requested accuracy (each edge was subdivided into 23).

The efficiency comparison is shown in Table B.2.

	linear elements	hp-elements
DOF	259393	6331
Error	1.617 %	1.521 %
Iterations	228	60
CPU time	**34 min.**	**11.58 sec.**

Table B.2 Comparison of the number of DOF, relative error in the H^1-norm, number of iterations of the matrix solver and the CPU-time.

B.2.6 Example 3: Sphere-cone problem

The next problem also deals with electrostatics. A metallic sphere of the radius 200 mm carries an electric potential φ_s = 100 kV. The distance of the sphere to the ground is 1000 mm. There is a metallic cone 100 mm above the sphere with zero electric potential. The cone is 500 mm high and its bottom has the radius 100 mm. The axisymmetric computational domain Ω is depicted in Fig. B.14 (notice that the figure describes the boundary conditions used). We solve the equation (7.27) in cylindrical coordinates again, and compare the performance of the piecewise-linear and hp-FEM. The solution, gradient of the solution and the meshes are shown in Figs. B.15 – B.19. An efficiency comparison is presented in Table B.3.

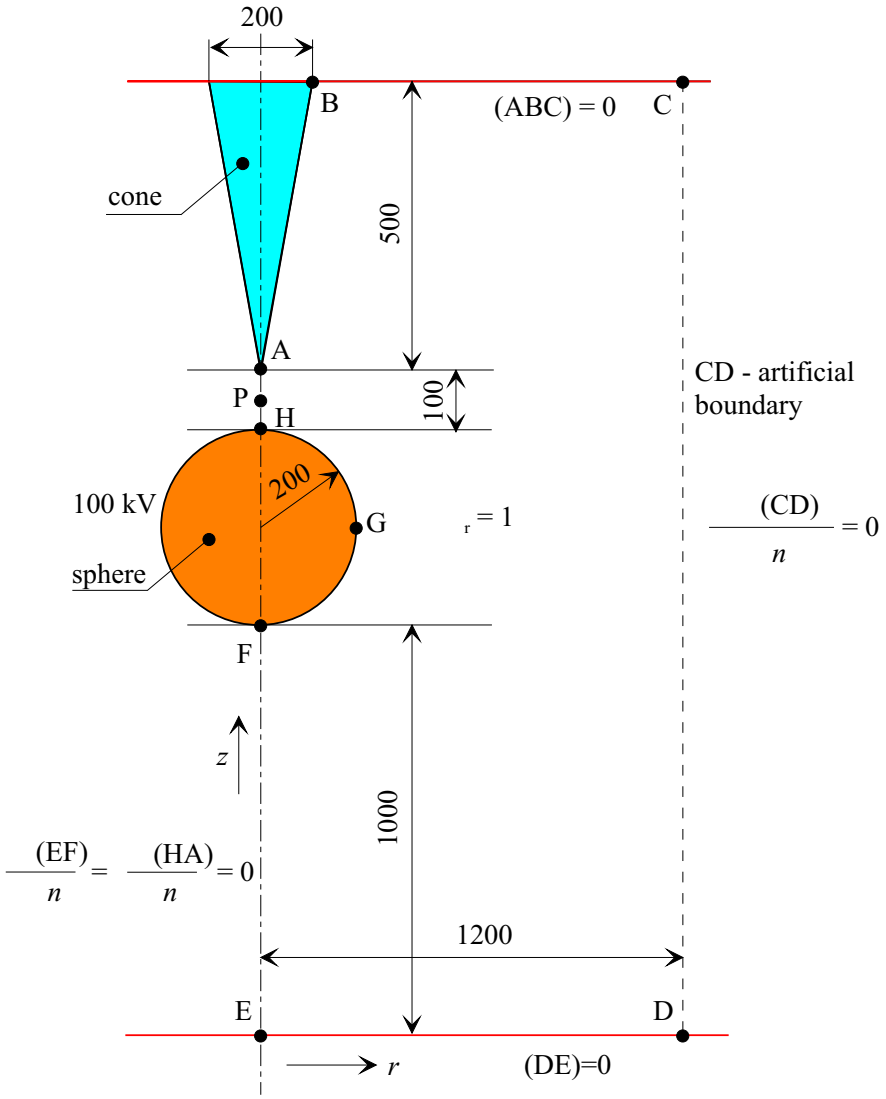

Figure B.14 Computational domain of the cone-sphere problem.

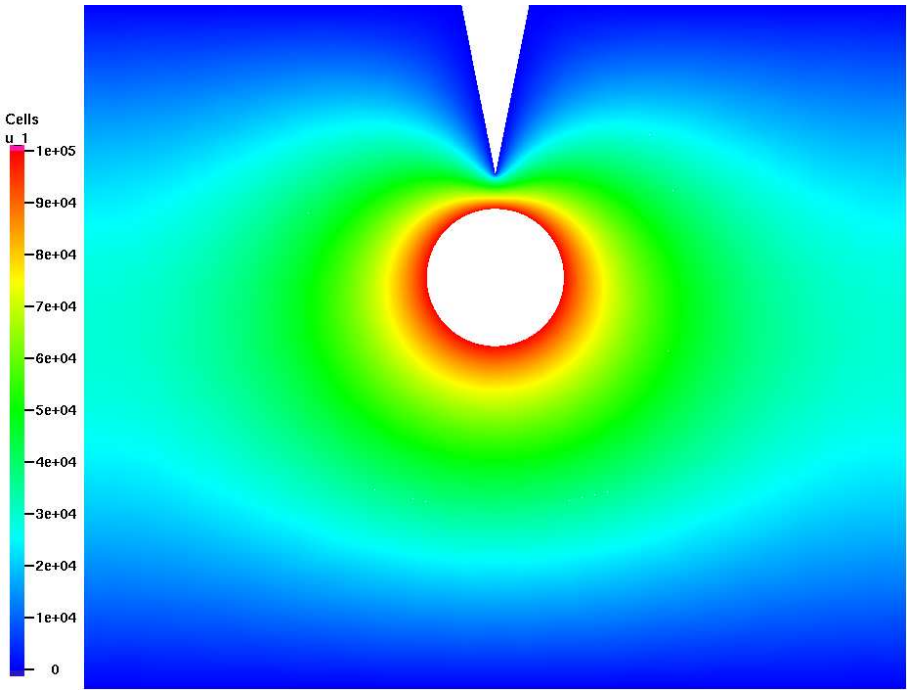

Figure B.15 Solution of the cone-sphere problem (the electric potential φ).

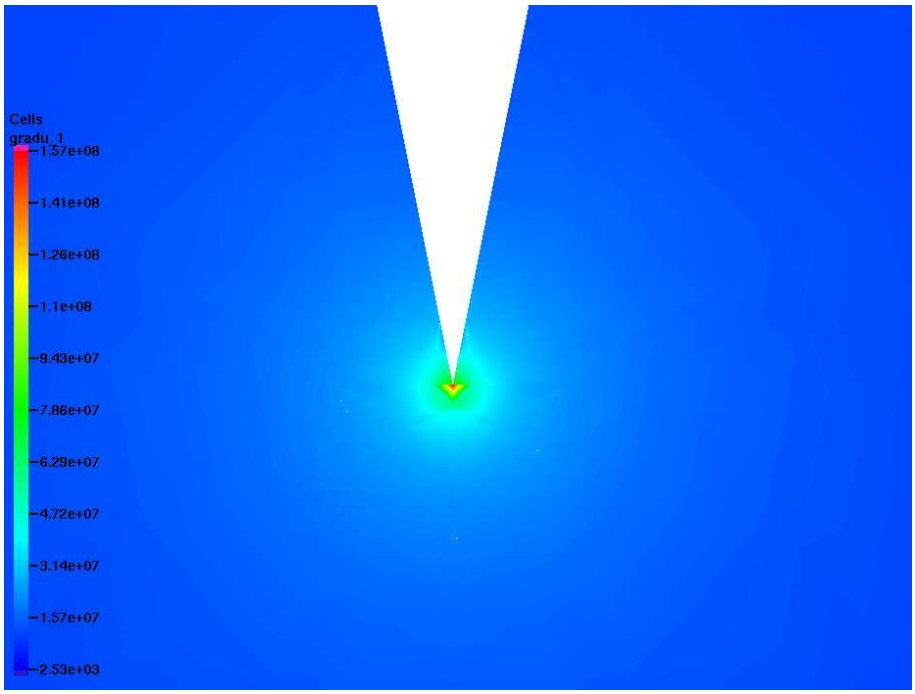

Figure B.16 Detail of the singularity of $|\boldsymbol{E}| = |-\nabla\varphi|$ at the tip of the cone (zoom = 100,000).

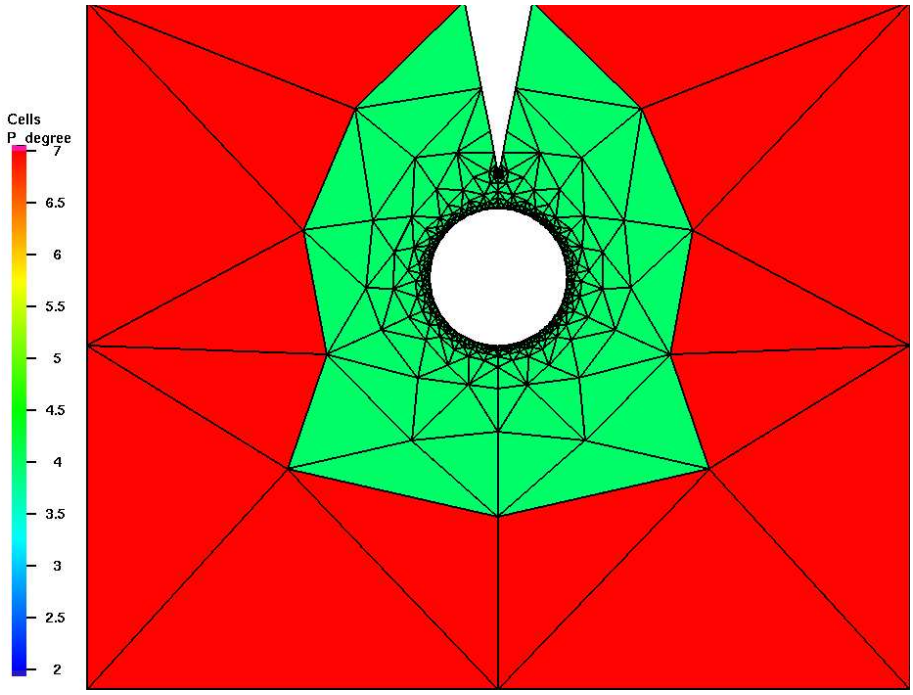

Figure B.17 The hp-mesh – global view. Large seventh-order elements are used far from the singularity and small quadratic elements at the tip of the cone.

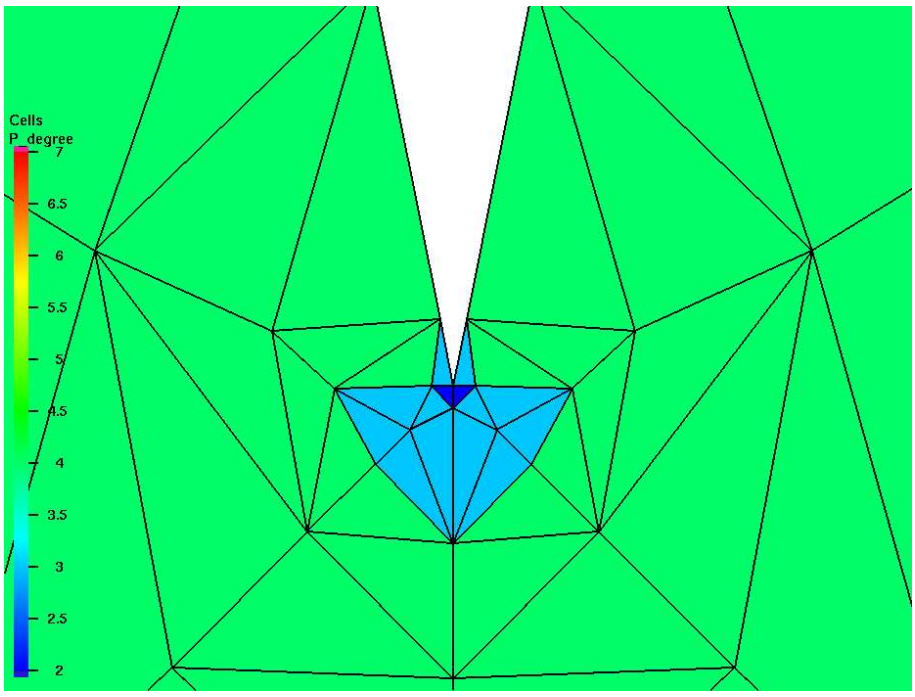

Figure B.18 The hp-mesh – detail of the tip of the cone (zoom = 100,000).

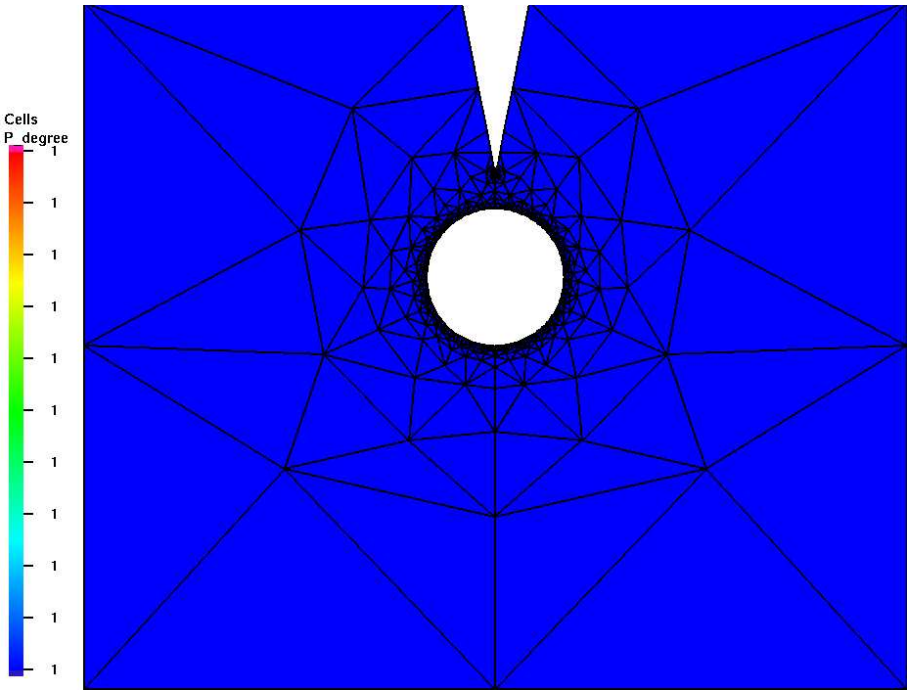

Figure B.19 The piecewise-linear mesh. This mesh was uniformly refined for the computation in order to attain the prescribed accuracy (each edge was subdivided into 48).

An efficiency comparison is shown in Table B.3.

	linear elements	hp-elements
DOF	488542	3317
Error	0.5858 %	0.2804 %
Iterations	859	44
CPU time	**30 min.**	**10.53 sec.**

Table B.3 Comparison of the number of DOF, relative error in the H^1-norm, number of iterations of the matrix solver and the CPU-time.

B.2.7 Example 4: Electrostatic micromotor problem

This computation is rooted in the construction of *electrostatic micromotors*. These devices, which are capable of transforming the electric energy into motion analogously to standard electromotors, do not contain any coils or electric circuits that could be destroyed by strong electromagnetic waves. The goal of this computation is a highly-accurate approximation of the distribution of the electric field in a domain containing two electrodes and a thin object placed between them. The problem is plane-symmetric, and Fig. B.20 shows one half of the domain Ω.

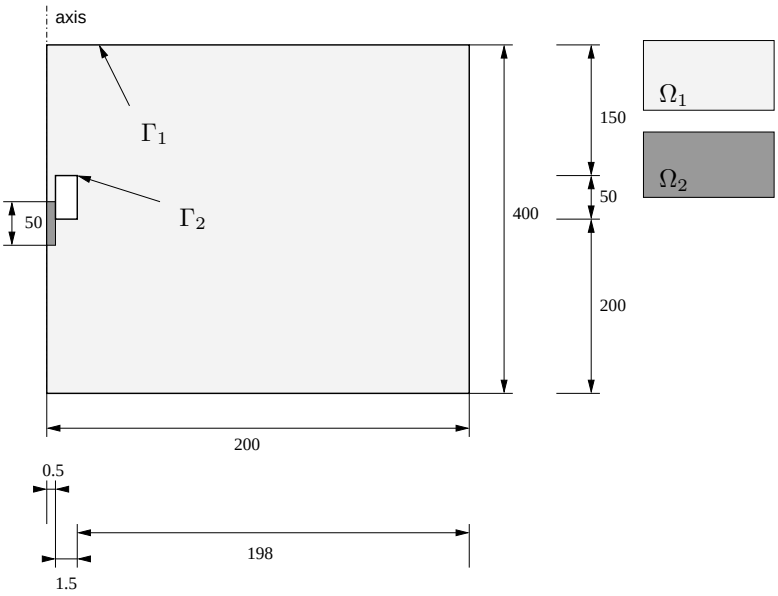

Figure B.20 Computational domain (the scaling was adjusted, but true measures in millimeters are provided). The electrode is modeled via a Dirichlet boundary condition.

The gray subdomain Ω_2 represents the moving part of the device, while the white subdomain Ω_2 represents the electrodes that are fixed. The distribution of the electric potential φ is governed by the equation (7.27),

$$-\nabla \cdot (\epsilon_r(\boldsymbol{x})\nabla\varphi(\boldsymbol{x})) = 0 \qquad \text{in } \Omega,$$

equipped with the Dirichlet boundary conditions

$$\varphi = 0 \text{ V} \qquad \text{on } \Gamma_1,$$

and

$$\varphi = 50 \text{ V} \qquad \text{on } \Gamma_2.$$

The relative permittivity ϵ_r is piecewise-constant, $\epsilon = 1$ in Ω_1 and $\epsilon = 10$ in Ω_2. We solve the problem twice, using the piecewise-linear and hp-FEM. The solution, gradient of the solution, a-posteriori error estimate based on a reference solution (obtained on a uniformly hp-refined mesh) and the meshes are shown in Figs. B.21 – B.23. An efficiency comparison is presented in Table B.4.

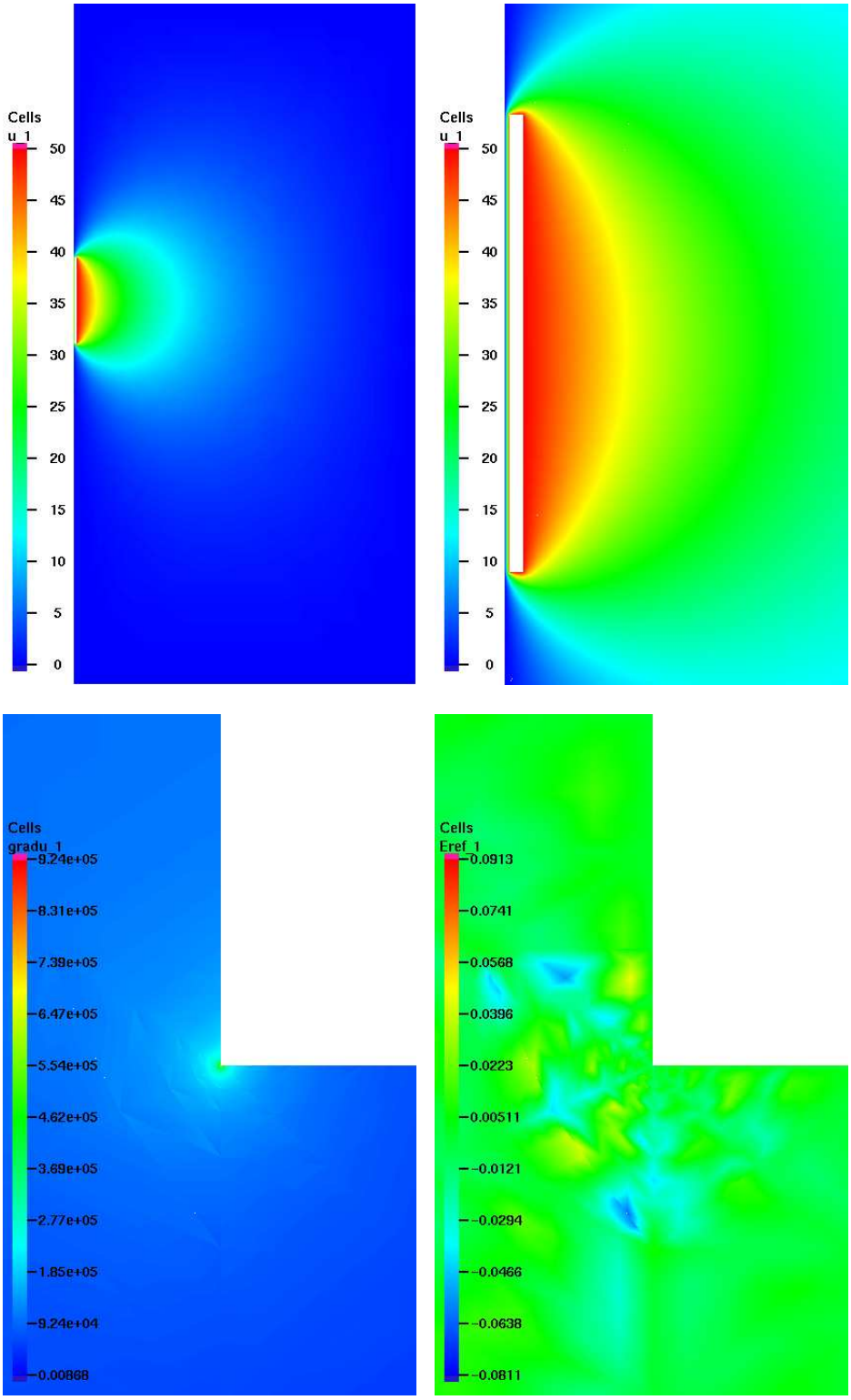

Figure B.21 Solution of the micromotor problem. Top: electric potential φ (zoom = 1 and 6). Bottom left: detail view of the singularity of $|\boldsymbol{E}| = |-\nabla\varphi|$ at a corner of the electrode (zoom = 1000). Bottom right: Error estimate based on a reference solution (zoom = 1000).

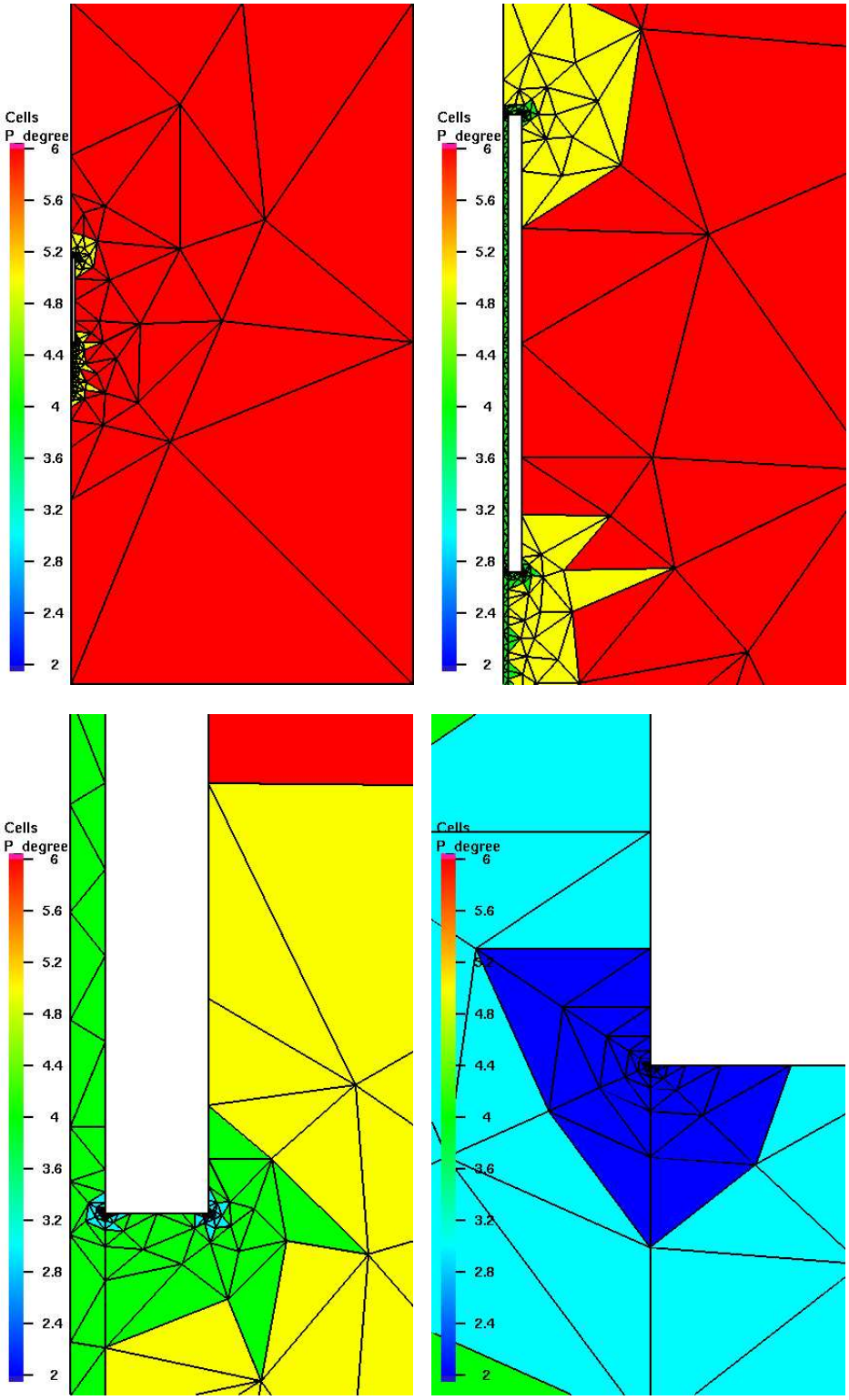

Figure B.22 The hp-mesh (zoom = 1, 6, 50, 1000). Large sixth-order elements are used far from the electrodes and small quadratic elements are placed at the re-entrant corners.

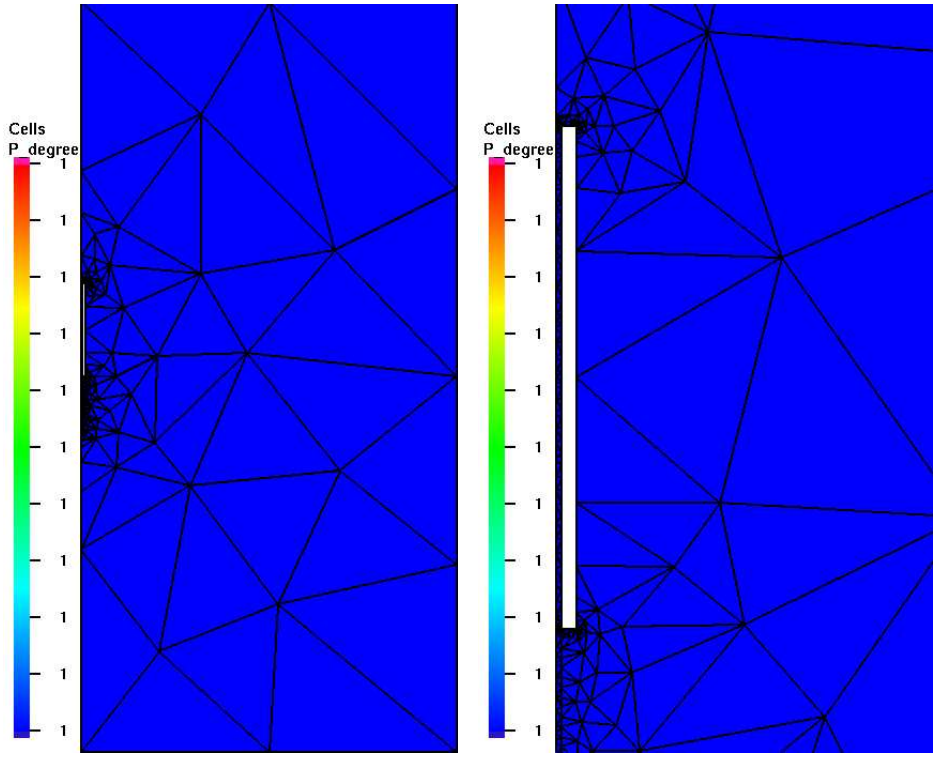

Figure B.23 This piecewise-linear mesh was uniformly refined for the computation in order to achieve the requested accuracy (each edge was subdivided into 44) (zoom = 1 and 6).

An efficiency comparison is shown in Table B.4.

	linear elements	hp-elements
DOF	472384	4511
Error	0.2024 %	0.173 %
Iterations	387	71
CPU time	**32 min.**	**17 sec.**

Table B.4 Comparison of the number of DOF, relative error in the H^1-norm, number of iterations of the matrix solver and the CPU-time.

B.2.8 Example 5: Electromagnetics diffraction problem

The last example taken from [76] is concerned with an electromagnetic diffraction problem in the domain $\Omega = (-10, 10)^2 \setminus (0, 10) \times (-10, 0)$ with re-entrant corner. The Maxwell's module of HERMES (see Paragraph B.2.3) is employed to discretize the time-harmonic Maxwell's equations by means of hierarchic hp edge elements. The edge elements use the same hp-FEM kernel as the elliptic module that was described in Paragraph B.2.2. The technology of the hierarchic edge elements is slightly different from the Nédélec elements. The hierarchic vector-valued shape functions used in HERMES can be found in [111]. The reference transformation (7.115) derived in Paragraph 7.5.2 is used without changes.

The problem involves perfect perfect conducting boundary conditions on the edges meeting at the re-entrant corner, and impedance boundary conditions on the rest of the boundary (see [76] for their exact definition). The exact solution to this problem is given by

$$\boldsymbol{E}(\boldsymbol{x}) = \bar{\nabla} \times J_\alpha(r) \cos(\alpha\phi), \qquad r(\boldsymbol{x}) = \sqrt{x_1^2 + x_2^2}, \tag{B.8}$$

where the symbol $\bar{\nabla} = (\partial/\partial x_2, -\partial/\partial x_1)^T$ stands for the vector-valued curl, $\alpha = 2/3$, J_α is the Bessel function of the first kind, and (r, ϕ) are the cylindrical coordinates in the plane. The exact solution (whose singularity was truncated for visualization purposes) is depicted in Fig. B.24. We do not show the approximate solutions, since they are optically identical to the exact one. Figs. B.25 and B.26 show the hp-mesh and lowest-order mesh consisting of the Whitney elements. An efficiency comparison is shown in Table B.5.

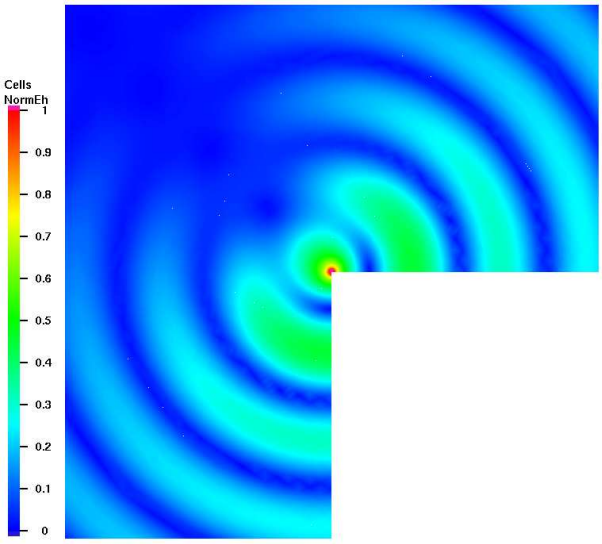

Figure B.24 The exact solution to the diffraction problem (the magnitude of the phasor of the electromagnetic field $|\boldsymbol{E}|$). The singularity at the re-entrant corner was truncated for visualization purposes.

This example can be used to make another important observation: The asymptotic expansion of the exact solution (B.8) at $r = 0$ reveals a singularity $O(r^{-4/3})$, which is too strong for $\boldsymbol{E}$ to lie in the space $[H^1(\Omega)]^2$. Thus, getting back to what we said at the beginning of Section 7.5, no Galerkin sequence could be constructed using subspaces of $[H^1(\Omega)]^2$.

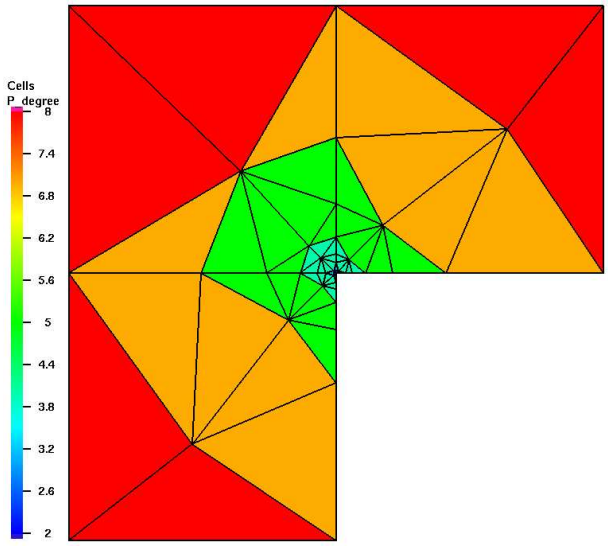

Figure B.25 The hp-mesh consisting of hierarchic edge elements.

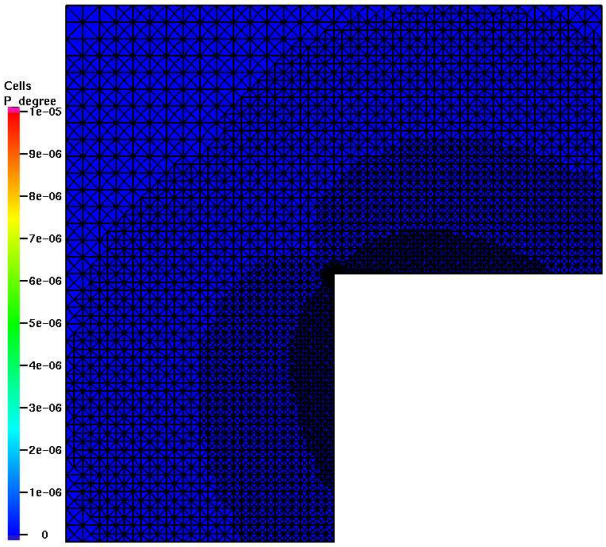

Figure B.26 The mesh consisting of the lowest-order (Whitney) edge elements. This mesh was uniformly refi ned for the computation (each edge was split into 10).

	Whitney edge elements	hp edge elements
DOF	2586540	4324
Error	0.6445 %	0.6211 %
CPU time	**21.2 min.**	**2.49 sec.**

Table B.5 Comparison of the number of DOF, relative error in the $H(\mathrm{curl})$-norm and the CPU-time.